12 YEARS OF ATMOSPHERIC MONITORING BY THE PLANETARY FOURIER SPECTROMETER ONBOARD MARS EXPRESS

Marco Giuranna[1], [1]Institute for Space Astrophysics and Planetology (IAPS), National Institute of Astrophysics (INAF), Via del Fosso del Cavaliere 100, 00133 Roma, Italy (marco.giuranna@iaps.inaf.it), **P. Wolkenberg**[1,2], [2]Space Research Centre of Polish Academy of Sciences, Bartycka 18A, Warsaw, Poland, **D. Grassi**[1], **A. Aronica**[1], **S. Aoki**[1,3], [3]Department of Geophysics, Tohoku University, Sendai, Miyagi 980-8578, Japan, **V. Formisano**[1,†], **D. Scaccabarozzi**[4], **B. Saggin**[4], [4]Department of Mechanics, Politecnico di Milano, Campus of Lecco, via G. Previati 1c, 23900, Lecco, Italy

Introduction:

We used thermal-infrared spectra returned by the Mars Express Planetary Fourier Spectrometer (PFS-MEx) to retrieve atmospheric temperature profiles, surface temperatures, and column-integrated optical depths of dust and water ice. More than 2,500,000 spectra have been used to build this new dataset, covering the full range of season, latitude, longitude, and local time. The data presented here span more than six Martian years (from MY26, Ls = 331°, 10 January 2004 to MY 33, Ls = 78°, 6 December 2015). By exploiting PFS/MEx capability to perform observations at different local times (LT), this dataset allows investigation of the daily cycles of suspended dust and ice. We present an overview of the seasonal and latitudinal dependence of atmospheric quantities during the relevant period, as well as an assessment of the interannual variability in the current Martian climate. Daily variations of Martian aerosols are also presented, including dust during the global dust storm of MY 28, and water ice in the aphelion cloud belt. Atmospheric temperatures and aerosols opacity are successfully retrieved in the polar regions, including the polar nights. Effects of suspended dust on atmospheric temperatures is also investigated.

Retrieval algorithm and error estimates:

The atmospheric parameters presented here are retrieved by means of the algorithm for the scientific analysis of individual calibrated PFS measurements originally developed by [1]. The improved algorithm uses the optimal estimation method with the Bayesian approach [2], and has been optimized for the retrieval of dust opacity during strong dust storms. The total covariance matrix is output for each single retrieval to provide accurate error estimates. The variance of retrieved opacities appears to be strongly related to the values of the surface temperatures. Namely, large variances are observed for low surface temperatures (or, equivalently, for low signal-to-noise ratio spectra), as one would expect. An in-depth analysis revealed the dataset can actually be divided in two sub-datasets, based on the surface temperatures. The temperature threshold is found to be 220 K for dust and 210 K for ice. Two different populations of standard deviations exist in the two temperature regimes. In **Figures 1 and 2** we

show the histograms of the standard deviation for dust and ice retrievals.
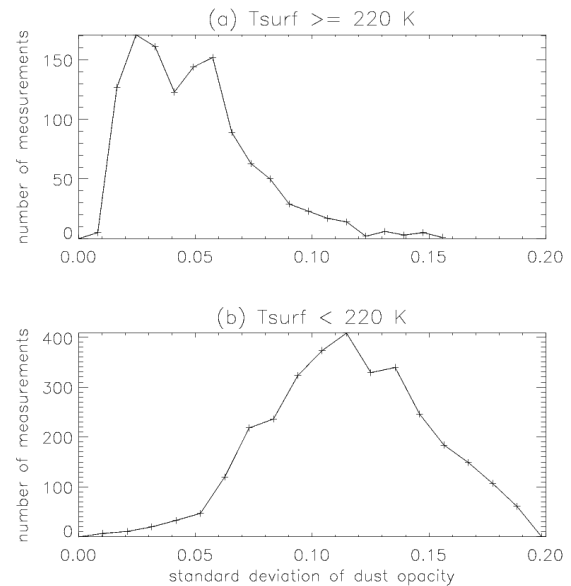

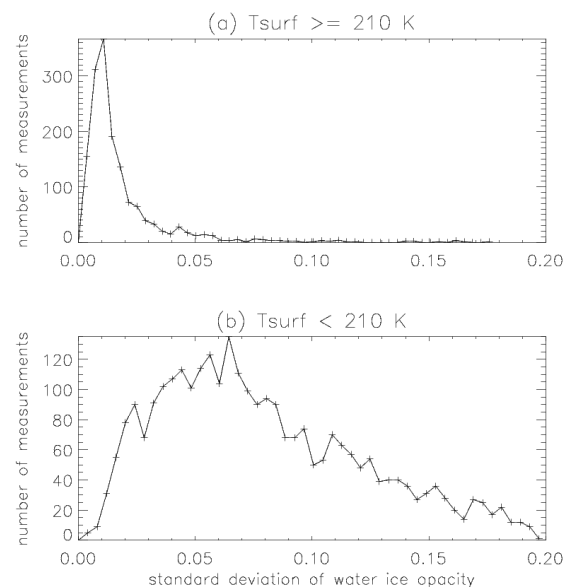**Fig.1** Histograms of the standard deviation for dust

Fig.2 Histograms of the standard deviation for ice

For both aerosols, the distribution peaks around small values in the "warm regime", with a typical standard deviation ranging from ~0.02-0.06 for dust (Fig. 1, top panel), and a sharp peak around 0.01 for

water ice (Fig. 2, top panel). On the other hand, in the "cold regime" the distribution's peak is observed at larger values, with a typical standard deviation of ~0.11 for dust (Fig. 1, bottom panel), and 0.06 or lower for water ice (Fig. 2, bottom panel).

The dataset:

In **Figure 3** we present the dataset of retrieved parameters for more than 6 full MYs. Repeatable patterns are observed every year for each of the retrieved quantities. A global dust storm occurred in MY 28. In contrast to a typical Martian year, the maximum of dust activity in this year occurs later, at ~ Ls = 270°, when zonally-averaged dust opacity exceeds 2 and atmospheric temperatures at 0.5 mb are about 30 degrees higher than the other years, where regional dust storm regularly occur. The strongest regional dust storm is observed in MY 29, in middle and polar latitude regions of both hemispheres.
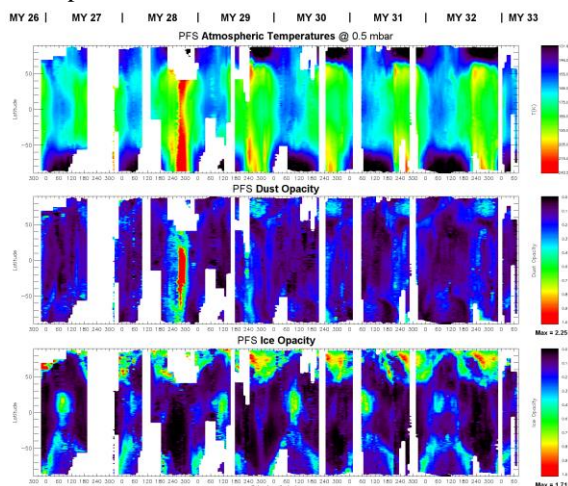

Fig.3 Zonal-mean atmospheric temperatures at 0.5 mbar (top), dust opacity (middle), and ice opacity (bottom) as a function latitude and Ls

Successful retrieval of dust and ice opacity in the polar regions. PFS observations allow the retrieval of atmospheric parameters in the polar regions, including the polar nights, where some of the most striking features are observed. In **Figure 4 and 5** we show the seasonal evolution of aerosols (average of full dataset, except data in the MY28 GDS). A region of extremely dust clear air generally separates the dust in the winter tropics from aerosol in the winter high latitudes (Fig. 4). This feature repeats every year in both hemispheres and has also been observed by MCS [3]. It cannot be reproduced by GCM models and a full explanation is still missing. An apparent increase of dust opacity is always observed at winter solstices in both polar regions. Also observed by MCS [3], this is likely CO_2 clouds retrieved as dust. The PFS retrieved water ice opacity in the polar regions reveals spatial and seasonal features that have not been observed before

(Fig. 5) and cannot be reproduced by current models, including recent implementations with improved microphysics and radiatively active ice clouds [4].
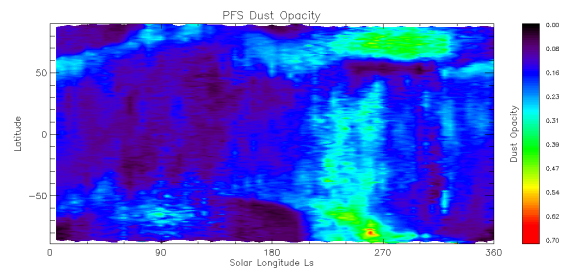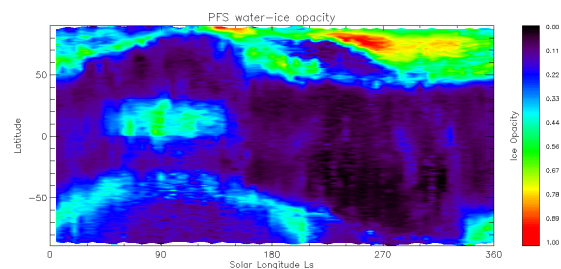

Fig.4 Seasonal evolution of dust opacity

Fig.5 Seasonal evolution of ice opacity

Climate, circulation and interannual variability. The spatial and temporal coverage of this dataset allows detailed analysis of the Martian climate and circulation. With six MYs currently covered by PFS observations, investigation of interannual variability of mean atmospheric parameters is also possible. The zonal-mean temperatures repeats very similarly on Mars each years, although interannual variations ranging from several up to tens of degrees can be observed (**Fig.6**).
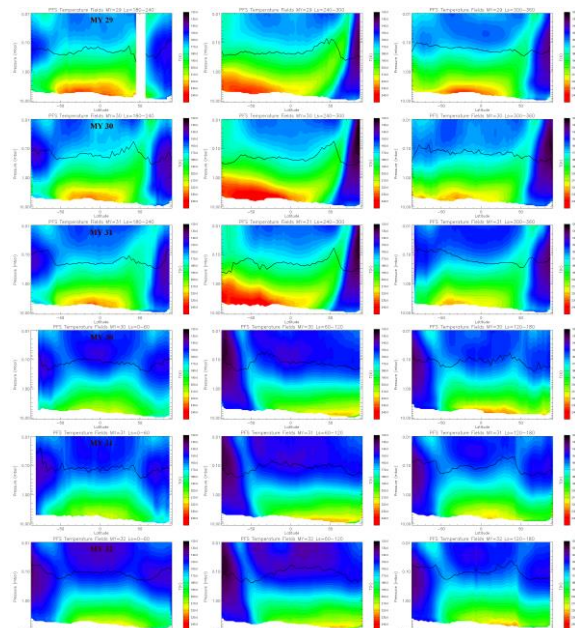

Fig.6 Zonal-mean temperatures for bins of 60° Ls. The logarithmic vertical scale is both for pressure and dust opacity (black solid line).

Such variations are often, although not exclusively, related to the overall dust content in the Martian atmosphere in the different years. Around the solstices (Ls = 90° and 270°, mid column in **Fig.6**), the atmospheric temperatures increase toward the pole at all levels in the summer hemisphere. The polar warming, caused by the adiabatic heating of air in the descending branch of the Hadley cell, is much stronger in the northern hemisphere then in the southern one. Being close to the time of perihelion (Ls = 251°), the Southern-hemisphere summer atmosphere shows much warmer temperatures than the Northern-hemisphere summer one. The thermal structure during the two equinox periods (Ls = 0° and 180° is nearly symmetric about the equator. This is a clear evidence of two main Hadley cells occurring on Mars in these periods. The region of extremely dust clear air appears to be located around the low-latitude periphery of the northern polar vortex.

Effects of dust on atmospheric temperatures. In **Figure 7** we compare atmospheric temperatures registered during the global dust storm event of MY28 with the temperatures observed for a typical Martian year (e.g., MY 30), when regional dust storms occur in the same range of Ls (240-300°).
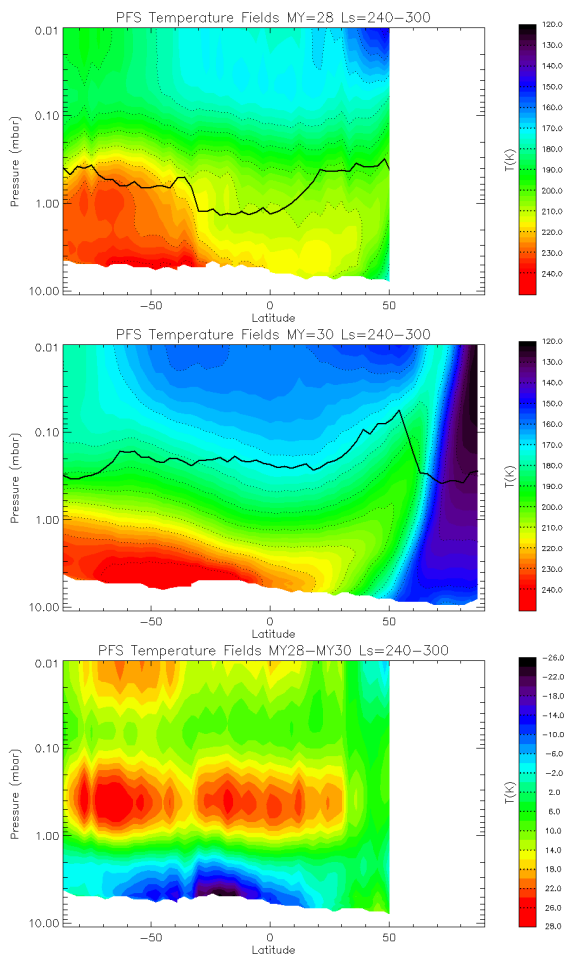

Fig.7 Effect of MY28 dust storm on temperatures.

The atmosphere is strongly heated up by absorption of solar radiation due to dust, as expected. During the planet-encircling dust storm of MY28, a net heating is observed for altitudes above the thickest dust layers, where the atmosphere is up to 28 K warmer than for a typical Martian year. However, the infrared radiative cooling rates due to dust cannot be overlooked in the lower altitudes within dusty atmosphere. Especially, at a dust storm event, cooling in the infrared regions is comparable to heating due to absorption of the incident solar radiation by dust, and the thermal structure of the Martian atmosphere is determined by the balance between heating and cooling caused by radiative effects of dust. Solar shielding by thick dust layers may also contribute to the cooling of the lower atmospheric layers. The region of maximum cooling corresponds to the region where maximum dust opacity is observed (0-30° S latitude; top and bottom panels of **Fig. 7**). Our result also indicates that even at out-of-storm events, cooling rate due to dust seems to have the same order as the magnitude of infrared radiative cooling due to CO_2 [6].

Daily cycles of dust and ice:

Contrary to TES and MCS data, the PFS dataset presented here allow us to investigate the daily variation of both ice and dust. Exploiting the non-Sun-synchronous nature of Mars Express orbit, PFS performed observations of Martian atmosphere at all local times .

Dust. The mean values of dust opacity during non-dusty seasons and during the global dust storm observed in 2007 will be presented as a function of local time for both hemispheres.

Ice. The aphelion cloud belt is composed of optically thin clouds that form above 10-15 km at low latitudes during northern spring and summer (Ls~50°-135°; [5]). The clouds form in the ascending branch of Hadley circulation north of the equator. In **Figure 10** we show the spatial distribution of nighttime and daytime ice clouds in the aphelion cloud belt as observed by PFS. There are strong similarities in the spatial distributions of the clouds, although the night clouds have higher opacity and are more extensive than the day clouds. Numerical modeling suggests that the tides are strongly influenced by topography [7] (primarily by Tharsis and Olympus mons) and thus water ice clouds are mainly found near the topographic features.

The daily variation of ice opacity in aphelion cloud belt observed by PFS will also be presented.

Conclusions:

With unprecedented spatial and temporal coverage and details revealed, this dataset offers new challenges to the GCMs and, at the same time, a new reference for the MYs complementary to those observed by MGS-TES.
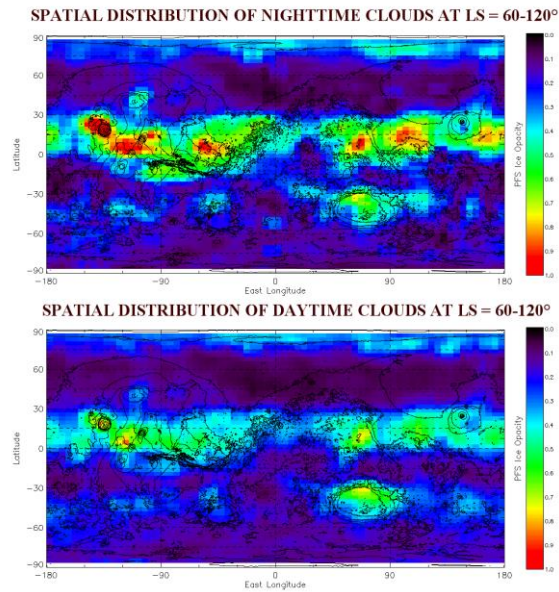
SPATIAL DISTRIBUTION OF NIGHTTIME CLOUDS AT LS = 60-120°

SPATIAL DISTRIBUTION OF DAYTIME CLOUDS AT LS = 60-120°

Fig.10 Spatial distributions of nighttime (top) and daytime (bottom) ice clouds in the aphelion cloud belt. Black contours are topography from MOLA.

References:

[1] D. Grassi, et al. (2005). Planet. Space Sci., 53, doi:10.1016/j.pss.2005.01.006.

[2] C.D. Rodgers (2000). Inverse Methods for Atmospheric Sounding: Theory and Practice, World Scientific, Singapore.

[3] N.G Heavens, et al. (2011). J. Geophys. Res., 116, E01010, doi:10.1029/2010JE003713.

[4] T. Navarro, et al (2014). J. Geophys. Res., 116, E01010, doi:10.1029/2010JE003713.

[5] R.T. Clancy, et al. (1996), Icarus, 122, doi:10.1006/icar.1996.0108.

[6] P. Wolkenberg et al. (2016). This workshop.

[7] D.P. Hinson, R.J Wilson. (2004). J. Geophys. Res., 109, E01002, doi:10.1029/2003JE002129.